Valley Vortex States and Degeneracy Lifting via Photonic Higher-Band Excitation

Daohong Song,[1,2] Daniel Leykam,[3,*] Jing Su,[1] Xiuying Liu,[1] Liqin Tang,[1] Sheng Liu,[4]
Jianlin Zhao,[4] Nikolaos K. Efremidis,[5] Jingjun Xu,[1,2,†] and Zhigang Chen[1,2,6,‡]

[1]*The MOE Key Laboratory of Weak-Light Nonlinear Photonics, and TEDA Applied Physics Institute and School of Physics,
Nankai University, Tianjin 300457, China*
[2]*Collaborative Innovation Center of Extreme Optics, Shanxi University, Taiyuan, Shanxi 030006, China*
[3]*Center for Theoretical Physics of Complex Systems, Institute for Basic Science, Daejeon 34126, Republic of Korea*
[4]*The Key Laboratory of Space Applied Physics and Chemistry, Ministry of Education and School of Science,
Northwestern Polytechnical University, Xi'an 710072, China*
[5]*Department of Mathematics and Applied Mathematics, University of Crete, 70013 Heraklion, Crete, Greece*
[6]*Department of Physics and Astronomy, San Francisco State University, San Francisco, California 94132, USA*

We demonstrate valley-dependent vortex generation in photonic graphene. Without breaking inversion symmetry, the excitation of two valleys leads to the formation of an optical vortex upon Bragg reflection to the third equivalent valley, with its chirality determined by the valley degree of freedom. Vortex-antivortex pairs with valley-dependent topological charge flipping are also observed and corroborated by numerical simulations. Furthermore, we develop a three-band effective Hamiltonian model to describe the dynamics of the coupled valleys and find that the commonly used two-band model is not sufficient to explain the observed vortex degeneracy lifting. Such valley-polarized vortex states arise from high-band excitation without a synthetic-field-induced gap opening. Our results from a photonic setting may provide insight for the study of valley contrasting and Berry-phase-mediated topological phenomena in other systems.

Valley pseudospin (VSP), manifesting the degenerate energy extrema of the bands in momentum space, is an intriguing fundamental concept that has stimulated tremendous interest. In recent years, light-valley interaction in two-dimensional (2D) materials has attracted a great deal of multidisciplinary interest in condensed matter physics and optoelectronics, largely due to its importance in fundamental physics and potential applications [1–3]. In particular, the VSP [or *valley degree of freedom* (VDF)] can be exploited to encode information for electrons just as the spin in spintronics, leading to a revitalizing field of "valleytronics," where a crucial step is to obtain pure valley-polarized states [4,5]. In 2D materials such as MoS_2, such valley-polarized electron states can be obtained by applying various external fields, which leads to different behavior due to the opposite Berry curvature of the two inequivalent valleys [2]. For example, when applying an electric field, the valley states of the electron can be spatially separated due to the valley Hall effect. Interestingly, the concept of the VDF and associated valley vortex states has been extended to classical wave systems involving artificial honeycomb lattices, ranging from optics to acoustics [6–13]. Such a utilization of the unique topological features of the valley states provides a new way to manipulate waves with robust transport properties. In these endeavors, various methods to achieve nontopological bulk valley transport as well as topological valley transport in domain walls have been demonstrated in various

systems [10–17]. Thus far, most studies on valley-polarized states have been realized in honeycomb lattices (HCLs) with inversion symmetry breaking or with other synthetic gauge fields that open a gap at the Dirac point.

Photonic graphene [18–22] serves as a compelling platform to emulate graphene and topological physics. The advantage of using a photonic system lies not only in its controllable structure parameters, but also in its Bloch modes with desired momentum that can be selectively excited and directly measured in both intensity and phase, enabling the exploration of fundamental phenomena which are otherwise inaccessible in real graphene materials. Indeed, a variety of intriguing phenomena have been observed in photonic HCLs in recent years, including, for example, unconventional edge states, Aharonov-Bohm-like interference, valley Landau-Zener-Bloch oscillations, and photonic topological insulators [12,23–28].

In this work, we demonstrate the generation of valley-contrasting vortices and vortex pairs in optically induced HCL with preserved lattice inversion symmetry [29]. Specifically, when two interfering Gaussian-like beams are mapped onto the same sublattice (in real space) but selectively excite two equivalent valleys (either K or K' in momentum space), a singly charged vortex emerges at the HCL output with its vortex chirality determined by the valley selection. Furthermore, valley-dependent vortex pairs are also observed when the two sublattices are equally excited. Numerical results are in excellent agreement with
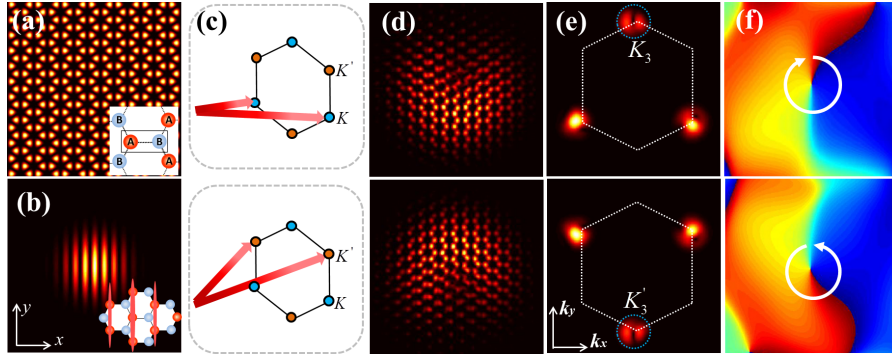
FIG. 1. Numerical simulation of pseudospin vortex states from valley-selective excitation. (a) The HCL composed of induced waveguides, where the inset illustrates sublattices A and B marked with red and blue dots, respectively. (b) The interfering probe beams used for lattice excitation, where the inset illustrates the excitation condition in real space. (c) Illustration of the excitation condition when the two K (top row) or K' (bottom row) valleys are selectively excited in momentum space. (d) Output intensity pattern of the probe beams. (e) Corresponding spectrum, where blue dashed circle marks the Bragg-reflected component and white dashed hexagon depicts the first BZ. (f) Phase structure of the Bragg-reflected component.

experimental observations, uncovering the charge flipping from decomposed two spinor components. In contradistinction to previously observed pseudospin states based on the *sublattice degree of freedom* (SDF) [26,30], the charge flipping based on the VDF occurs in the same spinor component. We emphasize that the excitation scheme and the physics studied here are different from our previous work [26] which focused only on the SDF. The VDF leads to fundamentally different pseudospin states of the graphene lattice. Importantly, we develop an effective Hamiltonian three-band model to describe the coupled valley dynamics and show that the presence of a third gapped band is essential to explain the observed vortex-pair states, although the gap itself remains closed at the Dirac points where a singular Berry curvature and pseudospin winding number is expected [31,32]. Such vortex degeneracy lifting without inversion symmetry breaking or a synthetic-field-induced gap opening may lead to a new understanding of VSP-mediated topological phenomena in other systems.

The dynamics of a probe beam propagating through the photonic HCL can be simulated by the following paraxial Schrödinger-type equation [33]:

$$i\frac{\partial\psi(x,y,z)}{\partial z} = -\frac{1}{2k_0}\nabla^2\psi(x,y,z)$$
$$-\frac{k_0\Delta n(x,y)}{n_0}\psi(x,y,z) \equiv H_0\psi, \quad (1)$$

where ψ is the field envelope of the probe beam, (x, y) are the transverse coordinates, z is the longitudinal propagation distance, k_0 is the wave number, n_0 is the refractive index of the medium, and $\Delta n(x, y)$ is the induced index change forming the HCL. In Eq. (1), H_0 is the continuous Hamiltonian of the system, whose eigenvalues are the wave vectors along the z direction (i.e., the propagation constant). The HCL is composed of two triangular sublattices A and B in real space [Fig. 1(a)], while in

momentum space the first two Floquet-Bloch bands intersect at the Dirac points located at the corners of the first Brillouin zone (BZ), namely, the K and K' valleys [see Fig. 1(b)], where the dispersion is linear [34]. Around the Dirac points, the Berry flux is π and $-\pi$ for the K and K' valleys, respectively, as measured in real graphene [35] or an artificial graphene system [36]. In order to detect the valley-contrasting phenomena, it is often necessary to break the lattice inversion symmetry, opening a gap at the Dirac points to examine the valley-dependent transport based on the Berry curvature [37]. In contrast, in what follows, we study the valley vortex states in a photonic HCL without breaking the inversion symmetry by directly measuring the phase structure of the valley states.

First, we numerically examine the valley-dependent vortex generation and topological charge flipping when inequivalent valleys of the HCL are selectively excited. Typical simulation results are shown in Fig. 1. The HCL, shown in Fig. 1(a), is uniform and thus has inversion symmetry, hosting gapless touching of the two bands at the Dirac points [18,19]. The probe beam, depicted in Fig. 1(b), is constructed by interfering two broad Gaussian beams, momentum matched to two Dirac points in the same (either K or K') valleys [Fig. 1(c)]. Here, we focus on the VDF in momentum space while keeping the same sublattice excitation in real space (e.g., sublattice A). After propagating through the HCL, the output probe beam exhibits asymmetrical conical diffraction. In particular, by comparing the output intensity patterns when exciting the K or K' valleys, we see that they are related by reflection symmetry. Although the probe beam excites only two Dirac points initially, the spectrum at the third equivalent Dirac point emerges at output due to Bragg reflection [see Fig. 1(e)]. Interestingly, such a Bragg-reflected component (extracted in Fourier space) contains a singly charged vortex with opposite chirality at K_3 and K_3', as can be seen clearly from the phase structure [Fig. 1(f)]. These results arise from the
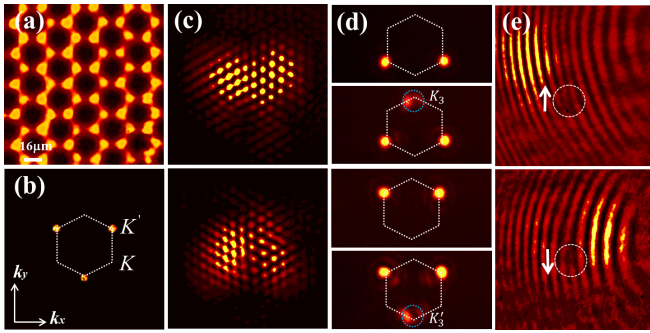
FIG. 2. Experimental demonstration corresponding to Fig. 1. (a) The HCL established by optical induction. (b) The k-space spectrum of the lattice beam, where K and K' valleys are marked. (c)–(e) Vortex generation when two K (top row) or K' (bottom row) valleys are selectively excited. (c) Output intensity patterns. (d) Input (top subpanel) and output (bottom subpanel) spectra, where blue dashed circles mark the newly generated spectral component at the third valley. (e) Interferograms from the Bragg-reflected components, where the vortex position or chirality is marked.
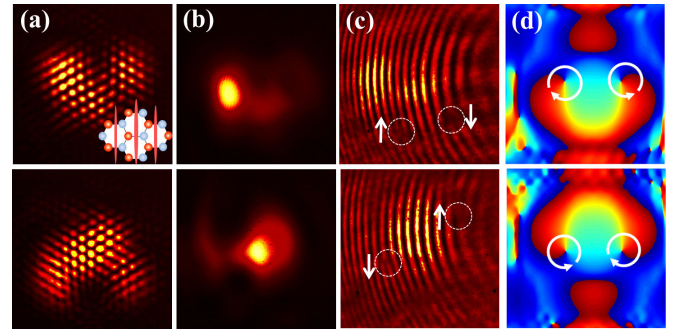
FIG. 3. Demonstration of valley-dependent vortex pair generation. The excitation scheme is the same as in Fig. 1 for K (top row) or K' (bottom row) valleys, except that the probe beam is shifted to the intersite position [see the inset in (a)]. (a) Output intensity patterns. (b) Far-field patterns of Bragg-reflected component from the third valley. (c) Interferograms of (b) with an inclined plane wave, where the vortex pair is marked. (d) Numerically calculated phase of the Bragg-reflected component showing the vortex pair of opposite chirality.

VDF, in contrast to the SDF-mediated vortex states obtained under different excitation conditions [38]. Remarkably, as we shall see, we obtained also similar experimental results (in terms of output intensity and phase structure) despite the very different physics involved.

Next, we present experimental results of such valley-dependent vortex states. The setup is similar to that used in our previous work on sublattice-mediated vortex generation [26,38] except that now the excitation conditions are different. The HCL is optically induced in a 10-mm-long biased photorefractive SBN crystal illuminated with a triangular lattice beam. When applying a negative voltage (about 1.4 kV/cm) across the crystalline c axis, the lattice beam experiences a self-defocusing nonlinearity, which transforms the triangular intensity pattern into the HCL index potential [18,23,39]. For this study, the lattice spacing is about 16 μm as shown in Fig. 2(a). The k-space spectrum of the lattice beam is shown in Fig. 2(b), where K and K' valleys are located at the corners of the white dashed lines. The probe beam is constructed by interfering two broad Gaussian beams with their launching angles aligned to match two K (or two K') valleys, as illustrated in Fig. 1(c).

Typical results from the valley-dependent excitations are shown in Figs. 2(c) and 2(d). As in the simulation results in Fig. 1(d), the output patterns are asymmetric with a mirror reflection symmetry for different valley excitations. Because of the limited propagation distance (limited by the crystal), the output patterns in Fig. 2(c) cannot evolve into a symmetric conical diffraction pattern, which were achieved by three-beam excitation (momentum matched to three equivalent Dirac points) as shown in Ref. [26]. The Bragg-reflected components at the K_3 or K'_3 valley are marked with blue dashed circles in the bottom subpanels in Fig. 2(d). In order to measure the phase of this newly generated component, an inclined reference beam is

introduced to interfere with the far-field intensity pattern extracted from the K_3 or K'_3 valley. The resulting interferograms clearly display a single fork bifurcation towards opposite directions as shown in Fig. 2(e), indicating opposite topological charges. These results agree well with the simulation results shown in Fig. 1(f). Note that the probe beam excites the same sublattice A for both cases; thus, the charge flipping observed here is not due to the SDF [26] but rather the VDF. Interestingly, momentum-space vortices have been observed in plasmonic structures as winding of polarization vectors [40].

In addition to the above singly charged vortex, a valley-dependent vortex-antivortex pair and associated topological charge flipping are also observed. Experimentally, this is realized when both sublattices are equally excited, by launching the probe beam halfway between the two sublattices [see the inset in Fig. 3(a)]. The results for such a vortex pair generation are summarized in Fig. 3, where Fig. 3(a) shows the overall output intensity patterns, whereas Fig. 3(b) shows the far-field intensity patterns from the newly generated K_3 (top panel) or K'_3 (bottom panel) component. Although these intensity patterns are not dramatically different, their phase structure unveils new information. The interferograms from the Bragg-reflected components exhibit clearly two (instead of one) separate fringe bifurcations towards opposite directions as shown in Fig. 3(c). Moreover, the chirality of the pairing vortices is reversed when the excitation switches from the K valleys to the K' valleys. These results demonstrate clearly valley-dependent charge flipping of the vortex pair when both sublattices are equally excited, as observed also in numerical simulations [Fig. 3(d)]. The difference in the vortex position between experiments and simulations is attributed to the lattice inhomogeneity and/or imperfect excitation conditions in the experiment. We emphasize again that the
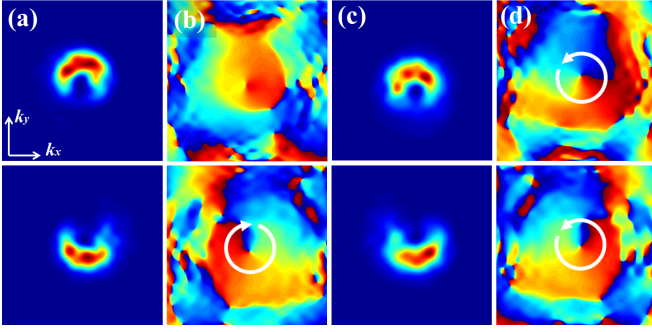
FIG. 4. Numerical projection of Bragg-reflected field into two spinor components when two K valleys are selectively excited. The top row corresponds to on-site excitation (Figs. 1 and 2) for single-vortex generation, and the bottom row corresponds to intersite excitation (Fig. 3) for vortex pair generation. (a),(b) Intensity and phase patterns of the sublattice ϕ_A component; (c), (d) corresponding results of the sublattice ϕ_B component. For excitation of two K' valleys, the topological charges for all vortices are reversed.

results in Figs. 2 and 3 arise from the VDF rather than the SDF presented in Ref. [38], and they are different results from different experiments revealing fundamentally different physics.

When modeling the SDF, it is often helpful to decompose the optical field into the two sublattices or spinor components $\psi = (\psi_A, \psi_B)$ [26]. In a similar fashion, the valley vortex states can be written in the spinor form: $\phi = (\phi_A, \phi_B)$, where ϕ_A and ϕ_B are the Fourier transformation of ψ_A and ψ_B, respectively. By solving Eq. (1), we obtain the intensity and phase of the two spinor components numerically for the K-valley vortex states, as shown in Fig. 4, where the two components have similar asymmetric intensity patterns but different phase structures. The top panels are derived from *on-site* excitation, where the ϕ_A component has a flat phase structure [Fig. 4(b)] but the ϕ_B component manifests a singly charged vortex [Fig. 4(d)]. Thus, the superposition of two spinor components leads to a singly charged vortex at the K_3 valley, in agreement with Fig. 2(e). On the other hand, the bottom panels are from *intersite* excitation for vortex-pair generation. In this case, each spinor component has a singly charged vortex but with opposite chirality [Figs. 4(b) and 4(d)], and thus the superposition leads to a vortex pair, as observed in Fig. 3(c). For the K' valley vortex states, the chirality of all spinor vortices is reversed due to time-reversal symmetry. Note that, for the SDF-induced vortex states, the topological charge flipping occurs in

two different spinor components while only one sublattice is excited [26], but for the VDF-mediated vortex states, it occurs in the same sublattice spinor component. Interestingly, from the results shown in Fig. 3, the valley vortex pair is generated with the two vortices well separated at the output, whereas from the sublattice decomposition analysis the vortices in the two components seem to overlap, suggesting the vortices should be degenerate. The vortex degeneracy can be lifted if the HCL is deformed [27,28], but in our case it is not. The underlying physics of such vortex pairs certainly merits further investigation.

Thus, we develop a theoretical model to directly analyze the wave dynamics in momentum space. As the HCL is established by self-defocusing nonlinearity in the experiment, the index lattice potential can be written as [18,21] $2k_0^2 \Delta n/n_0 = -V(e^{iG_1 \cdot r} + e^{iG_2 \cdot r} + e^{i(G_1+G_2) \cdot r} + \text{c.c.})$, where $G_{1,2} = \frac{2\pi}{a}[(1/\sqrt{3}), \pm 1]$ and $G_3 \equiv G_1 + G_2$ are the reciprocal lattice vectors. Introducing the normalized propagation distance $\tilde{z} = 2k_0 z$ and expanding $\psi(r) = \int dp\, \psi(p) e^{ip \cdot r}$, the paraxial equation [Eq. (1)] can be Fourier transformed to obtain

$$i\partial_{\tilde{z}}\psi(p) = |p|^2 \psi(p) + V\sum_{j=1}^{3}[\psi(p - G_j) + \psi(p + G_j)], \quad (2)$$

where p is the wave packet momentum and V is a constant. The first term on the right-hand side forms a parabolic confining potential and accounts for the kinetic energy term, while the second term describes coupling to the six neighboring reciprocal lattice points. Thus, the Fourier space propagation resembles the tight-binding dynamics of a hexagonal lattice with a superimposed parabolic potential.

If the lattice potential is weak, the parabolic confining potential $|p|^2$ dominates and thus suppresses the scattering to higher BZs. Therefore, we can restrict our attention to the beam dynamics within the first BZ, in particular, the coupling between the three equivalent valleys $K_{1,2,3}$, where $K_1 = \frac{2\pi}{a}[-(1/\sqrt{3}), -\frac{1}{3}], K_2 = K_1 + G_1 + G_2$, and $K_3 = K + G_1$ are the positions of the equivalent Dirac points [41]. Assuming small displacements from the Dirac points, $p = K_{1,2,3} + \delta p = K_{1,2,3} + \delta p(\cos\theta, \sin\theta)$, the dynamics of the three coupled valleys can be described by an effective Hamiltonian: $i\partial_{\tilde{z}}\Psi(\delta p) = \hat{H}_{\text{eff}}\Psi(\delta p)$. After expanding the kinetic energy term, the effective Hamiltonian can be written as

$$\hat{H}_{\text{eff}}(\delta p) = p_0^2 + \delta p^2 + \begin{pmatrix} -\frac{4\pi}{3}\delta p(\sqrt{3}\cos\theta + \sin\theta) & V & V \\ V & \frac{4\pi}{3}\delta p(\sqrt{3}\cos\theta - \sin\theta) & V \\ V & V & \frac{8\pi}{3}\delta p\sin\theta \end{pmatrix}, \quad (3)$$

which describes the dynamics in the coupled valleys $K_{1,2,3}$. For K' valleys, the only difference is the sign in the $\sin\theta$ term, which corresponds to the y component of the displacement from the valleys. At large momenta, this model exhibits trigonal warping of the Dirac cones, which can lift the valley degeneracy [42].

For this effective model, the Dirac point lies at $\delta p = 0$, where the eigenvalues of the Hamiltonian matrix $\hat{H}_{\text{eff}}$ are $-V$, $-V$, and $2V$ with corresponding eigenvectors $|u_1\rangle = (-1, 1, 0)$, $|u_2\rangle = (-1, 0, 1)$, and $|u_3\rangle = (1, 1, 1)$, where $|u_{1,2}\rangle$ are the degenerate Dirac point eigenstates

while $|u_3\rangle = (1, 1, 1)$ is the eigenstate of a third (gapped) band. Roughly speaking, this third band describes intersite excitations between waveguides (i.e., the antiguiding modes), which is the case for the excitation of valley vortex pairs as shown in Fig. 3.

We can construct pseudospin eigenstates as the rotationally symmetric superposition of $|u_{1,2}\rangle$, i.e., $|u_{\pm}\rangle = (1, e^{\pm i 2\pi/3}, e^{\mp i 2\pi/3})$. To verify that this is the correct form of the pseudospin eigenstates, we rewrite $\hat{H}_{\text{eff}}$ in the basis formed by $(|u_+\rangle, |u_-\rangle, |u_3\rangle)$:

$$\hat{H}_{\text{spin basis}} = p_0^2 + \delta p^2 - \begin{pmatrix} V & \frac{2\pi}{3}(\sqrt{3}+i)\delta p e^{-i\theta} & \frac{2\pi}{3}(\sqrt{3}-i)\delta p e^{i\theta} \\ \frac{2\pi}{3}(\sqrt{3}-i)\delta p e^{i\theta} & V & \frac{2\pi}{3}(\sqrt{3}+i)\delta p e^{-i\theta} \\ \frac{2\pi}{3}(\sqrt{3}+i)\delta p e^{-i\theta} & \frac{2\pi}{3}(\sqrt{3}-i)\delta p e^{i\theta} & -2V \end{pmatrix}. \tag{4}$$

If we assume the third band is not excited and can be neglected (i.e., in the tight-binding limit of a deep lattice potential—not really the case for our experiment), then the above equation turns into the familiar massless two-band Dirac Hamiltonian.

To compare with the valley vortex experiment, we excite two equivalent valleys with a tunable relative phase between them; i.e., the initial state is $\Psi = e^{-\delta p^2 w^2}(1, e^{i\varphi}, 0)$, where w is the beam width and φ determines the position of the peak amplitude associated with the beam in real space. The beam has a peak at the space between waveguides when $\varphi = 0, \pi$ (as in the case of intersite excitation in the experiment) but on one of the sublattices when $\varphi = \pm 2\pi/3$ (as in the case of on-site excitation in the experiment). Note that the two-beam excitation always excites the third band $|u_3\rangle$, except for the special case $\varphi = \pi$.

We excite only one sublattice by setting $\varphi = 2\pi/3$ and compute the field scattered into the third (initially unexcited) valley by solving Eq. (4). The calculated phase and intensity is shown in Fig. 5, in good agreement with the experimental results. Swapping the valley index (while keeping the sublattice fixed) flips the topological charge,

leading to the generation of a vortex-antivortex pair. The vortex degeneracy is lifted by the emergence of the third band mode due to the off-site excitation, in addition to the modes at the vicinity of Dirac points. So our effective model can explain the experimental observations and capture the essential physics behind the vortex generation. To apply a two-band approximation, one must project the initial state onto the Dirac cone modes of $\hat{H}_{\text{eff}}$. However, doing so results in a nonzero input field amplitude at the third Dirac point. Basically, the input wave packet momentum $\boldsymbol{p}$ and the propagation constant or energy eigenvalue k_z do not commute; i.e., the plane wave or Gaussian inputs at one or two K points are not Bloch wave eigenstates, which excite all three K points.

In conclusion, we have demonstrated valley-dependent vortex generation and topological charge flipping in symmetry-preserving HCL. In contrast to the SDF, the VDF flips the topological charge in the same spinor component. Moreover, the valley vortex pair generation is achieved due to the lifting of the spinor vortex degeneracy arising from the excitation of the higher band modes, as explained by the momentum-space three-band model. Our results show clearly that valley-polarized states can be realized in HCL without inversion symmetry breaking or other synthetic gauge fields to open the gap at the Dirac point and that the commonly used two-band model is not always sufficient in the study of graphene-related physical phenomena. Thus, we believe our work should provide insight in the areas of valley physics in both condensed matter and artificial graphene systems.
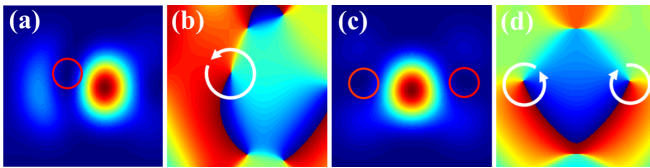

FIG. 5. Calculated intensity and phase of the Bragg-reflected field into the third valley from the three-band model. (a)–(d) Shown are the results obtained by solving the effective propagation of Eqs. (3) and (4) using normalized parameters $\tilde{z} = 0.5$ and $V = 1$, with a width beam $w = 0.8$. (a),(b) For on-site excitation to generate a single vortex (corresponding to Figs. 1 and 2). (c),(d) For intersite excitation to generate a vortex-antivortex pair (corresponding to Fig. 3).

*Corresponding author.
dleykam@ibs.re.kr
†Corresponding author.
jjxu@nankai.edu.cn
‡Corresponding author.
zgchen@nankai.edu.cn

[1] K. F. Mak, D. Xiao, and J. Shan, Nat. Photonics **12**, 451 (2018).

[2] X. Xu, W. Yao, D. Xiao, and T. F. Heinz, Nat. Phys. **10**, 343 (2014).

[3] J. R. Schaibley, H. Yu, G. Clark, P. Rivera, J. S. Ross, K. L. Seyler, W. Yao, and X. Xu, Nat. Rev. Mater. **1**, 16055 (2016).

[4] D. Xiao, W. Yao, and Q. Niu, Phys. Rev. Lett. **99**, 236809 (2007).

[5] A. Rycerz, J. Tworzydlo, and C. W. J. Beenakker, Nat. Phys. **3**, 172 (2007).

[6] J.-W. Dong, X.-D. Chen, H. Zhu, Y. Wang, and X. Zhang, Nat. Mater. **16**, 298 (2017).

[7] T. Ma and G. Shvets, New J. Phys. **18**, 025012 (2016).

[8] F. Deng, Y. Li, Y. Sun, X. Wang, Z. Guo, Y. Shi, H. Jiang, K. Chang, and H. Chen, Opt. Lett. **40**, 3380 (2015).

[9] X.-D. Chen, F.-L. Zhao, M. Chen, and J.-W. Dong, Phys. Rev. B **96**, 020202 (2017).

[10] J. Lu, C. Qiu, L. Ye, X. Fan, M. Ke, F. Zhang, and Z. Liu, Nat. Phys. **13**, 369 (2017).

[11] J. Lu, C. Qiu, M. Ke, and Z. Liu, Phys. Rev. Lett. **116**, 093901 (2016).

[12] J. Noh, S. Huang, K. P. Chen, and M. C. Rechtsman, Phys. Rev. Lett. **120**, 063902 (2018).

[13] F. Gao, H. Xue, Z. Yang, K. Lai, Y. Yu, X. Lin, Y. Chong, G. Shvets, and B. Zhang, Nat. Phys. **14**, 140 (2018).

[14] L. Ye, C. Qiu, J. Lu, X. Wen, Y. Shen, M. Ke, F. Zhang, and Z. Liu, Phys. Rev. B **95**, 174106 (2017).

[15] X. Wu, Y. Meng, J. Tian, Y. Huang, H. Xiang, D. Han, and W. Wen, Nat. Commun. **8**, 1304 (2017).

[16] X. Ni, D. Purtseladze, D. A. Smirnova, A. Slobozhanyuk, A. Alù, and A. B. Khanikaev, Sci. Adv. **4**, eaap8802 (2018).

[17] Y. Kang, X. Ni, X. Cheng, A. B. Khanikaev, and A. Z. Genack, Nat. Commun. **9**, 3029 (2018).

[18] O. Peleg, G. Bartal, B. Freedman, O. Manela, M. Segev, and D. N. Christodoulides, Phys. Rev. Lett. **98**, 103901 (2007).

[19] O. Bahat-Treidel, O. Peleg, M. Grobman, N. Shapira, M. Segev, and T. Pereg-Barnea, Phys. Rev. Lett. **104**, 063901 (2010).

[20] M. J. Ablowitz, S. D. Nixon, and Y. Zhu, Phys. Rev. A **79**, 053830 (2009).

[21] C. L. Fefferman and M. I. Weinstein, J. Am. Math. Soc. **25**, 1169 (2012).

[22] M. Polini, F. Guinea, M. Lewenstein, H. C. Manoharan, and V. Pellegrini, Nat. Nanotechnol. **8**, 625 (2013).

[23] Y. Plotnik et al., Nat. Mater. **13**, 57 (2014).

[24] M. C. Rechtsman, Y. Plotnik, J. M. Zeuner, D. Song, Z. Chen, A. Szameit, and M. Segev, Phys. Rev. Lett. **111**, 103901 (2013).

[25] M. C. Rechtsman, J. M. Zeuner, Y. Plotnik, Y. Lumer, D. Podolsky, F. Dreisow, S. Nolte, M. Segev, and A. Szameit, Nature (London) **496**, 196 (2013).

[26] D. Song, V. Paltoglou, S. Liu, Y. Zhu, D. Gallardo, L. Tang, J. Xu, M. Ablowitz, N. K. Efremidis, and Z. Chen, Nat. Commun. **6**, 6272 (2015).

[27] P. Zhang, D. Gallardo, S. Liu, Y. Gao, T. Li, Y. Wang, Z. Chen, and X. Zhang, Opt. Lett. **42**, 915 (2017).

[28] Y. Sun, D. Leykam, S. Nenni, D. Song, H. Chen, Y. D. Chong, and Z. Chen, Phys. Rev. Lett. **121**, 033904 (2018).

[29] D. Song, J. Su, X. Liu, S. Xia, D. Gallardo, L. Tang, J. Xu, and Z. Chen, in *Proceedings of the Conference on Lasers and Electro-Optics, San Jose, California, 2016* (Optical Society of America, Washington, DC, 2016), p. FTu1A.4.

[30] M. Mecklenburg and B. C. Regan, Phys. Rev. Lett. **106**, 116803 (2011).

[31] D. Xiao, M.-C. Chang, and Q. Niu, Rev. Mod. Phys. **82**, 1959 (2010).

[32] C.-H. Park and N. Marzari, Phys. Rev. B **84**, 205440 (2011).

[33] D. N. Christodoulides, F. Lederer, and Y. Silberberg, Nature (London) **424**, 817 (2003).

[34] A. H. Castro Neto, F. Guinea, N. M. R. Peres, K. S. Novoselov, and A. K. Geim, Rev. Mod. Phys. **81**, 109 (2009).

[35] Y. Liu, G. Bian, T. Miller, and T. C. Chiang, Phys. Rev. Lett. **107**, 166803 (2011).

[36] L. Duca, T. Li, M. Reitter, I. Bloch, M. Schleier-Smith, and U. Schneider, Science **347**, 288 (2015).

[37] R. V. Gorbachev et al., Science **346**, 448 (2014).

[38] D. Song, S. Liu, V. Paltoglou, D. Gallardo, L. Tang, J. Zhao, J. Xu, N. K. Efremidis, and Z. Chen, 2D Mater. **2**, 034007 (2015).

[39] Z. Chen, M. Segev, and D. N. Christodoulides, Rep. Prog. Phys. **75**, 086401 (2012).

[40] Y. Zhang, A. Chen, W. Liu, C. W. Hsu, B. Wang, F. Guan, X. Liu, L. Shi, L. Lu, and J. Zi, Phys. Rev. Lett. **120**, 186103 (2018).

[41] B. Terhalle, A. S. Desyatnikov, D. N. Neshev, W. Krolikowski, C. Denz, and Y. S. Kivshar, Phys. Rev. Lett. **106**, 083902 (2011).

[42] J. L. Garcia-Pomar, A. Cortijo, and M. Nieto-Vesperinas, Phys. Rev. Lett. **100**, 236801 (2008).